11th ANKARA INTERNATIONAL AEROSPACE CONFERENCE **AIAC-2021-138**
8-10 September 2021 - METU, Ankara TURKEY

UNSTEADY AERODYNAMICS OF CAMBERED AIRFOILS AT LOW REYNOLDS NUMBER

Tawfiq Ahmed[1] and Prof. Dr. Dilek Funda Kurtulus [2]
Middle East Technical University
Ankara, Turkey

ABSTRACT

Numerical simulations of cambered airfoils (NACA 1412, NACA 2412, NACA 3412) at Re = 1000 are investigated in the current study to understand the camber effect on unsteady aerodynamic behavior at low Reynolds number. The numerical simulations are performed at angles of attack ranging from 0° to 10°. The aerodynamic coefficients and flow fields are analyzed in detail.

INTRODUCTION

Most of the insects fly at Reynolds numbers of 10^3-10^4 and most of the birds fly at Reynolds number of 10^4 to 10^5 because of their low speed and small length scales [Shy, 2008]. Birds like hummingbirds fly at Re = O (10^4), on the other hand small insects like fruit flies or honeybees fly at Re = O (10^2 – 10^3) [Kang, 2013]. Mechanism like flapping wing Micro Air Vehicles (MAVs) need more favorable wing design for low Reynolds numbers in order to imitate the flights of birds and insects than fixed wing MAVs. Therefore, for the design of flapping wings Micro Air Vehicles (MAVs), the study of unsteady aerodynamics for different cambered airfoils at low Reynolds number is necessary.

In order to increase the knowledge of vortex shedding phenomena of flapping airfoils, knowledge of unsteady behavior of airfoils at low Reynolds numbers with steady external conditions is necessary. Most of the time these analytical models for flapping motions are based on quasi-steady approaches [Kurtulus, 2015]. Fundamental knowledge on physical characteristics of wing in steady condition is also important to understand the characteristics of the same wing in unsteady conditions. To understand perching and flapping airfoils, C_l- α, C_l-C_d relations on effective angle of attack are useful [Platzer, 2008].

A vortex formation study was conducted by Ohmi et al. [1990] both experimentally and numerically around an ellipse and a NACA 0012 airfoil oscillating and translating at Re=1500 to 10000. All the experiments were carried out in a water tank and the wake pattern were categorized as per the shedding and development of vortices as static stall type, synchronized shedding type, parallel shedding type, and vortex superposition type. Kurtulus et al. [Kurtulus, 2015] conducted an experiment using the same methodology but with a modified mechanism to investigate flow physics around pitching/plunging NACA 0012 airfoil at Re =1000.

[1] Prof. Dr. Dilek Funda Kurtulus, Email: funda.kurtulus@ae.metu.edu.tr
[2] Tawfiq Ahmed, Email: e194794@metu.edu.tr

Recently, perching maneuvers at low Reynolds number have gained some interests. The perching maneuver like a pitch-up problem, where the angle of attack varies over a large amplitude [Ol et al., 2009]. A previous study was conducted by Ol et al. [2009] to investigate the flow around flat plate and 10% thick ellipse at a constant pitch rate at Re = 100 and Re = 1000 at an amplitude from 0° to 40°. To control the MAVs and model the mechanism model the knowledge of the flow physics around micro air vehicles at steady conditions will contribute a lot especially in cases with perching, gust response, maneuvering flight and flapping wings.

It is important to understand the physics of flow separation and vortex formation because even at steady external conditions, wakes behind airfoils and bluff bodies at high angles of attack are unsteady [Gopinath, 2006]. As at low Reynolds number flow is laminar, mild adverse pressure gradient can cause separation to the flow.

A previous study on the effect of cambered airfoils NACA 0002 and NACA 4402 for Re = 1000, Re = 2000, Re = 6000 with angles of attack ranging from 0° to 10° has been conducted by Kunz et al. (2003) and they denoted that the camber increases the maximum lift-to-drag ratio for the Reynolds number range investigated [Kunz et al., 2003].

A detailed study on NACA 0012 at low Reynolds number of 1000 for angles of attack ranging from 0° to 90° gives a very good idea of the behavior of unsteady aerodynamics of the flow around a symmetric airfoil as the angles of attack increases [Kurtulus, 2015, 2016] and the wake of the symmetric airfoil has been distinguished to performed different modes depending on the angle of attack.

The same approach has been taken into account for the current study. The unsteady aerodynamics around 3 cambered airfoils is simulated at very low Reynolds number. Numerical analyses have been conducted around NACA 1412, NACA 2412, and NACA 3412 at Re = 1000 for angles of attack in the range of 0° to 10° using a finite-volume program ANSYS Fluent.

METHOD

Governing equations and geometry

Navier-Stokes equations for incompressible, laminar, and two-dimensional flow are given in Eq. 1 and Eq. 2:

$$\vec{\nabla}.\vec{V} = 0 \tag{1}$$

$$\frac{\partial \vec{V}}{\partial t} + \left(\vec{\nabla}.\vec{V}\right)\vec{V} = -\frac{1}{\rho}\vec{\nabla}p + \upsilon\nabla^2\vec{V} \tag{2}$$

where, $\vec{V}$ is the velocity, ρ is the fluid density, p is the pressure, υ is the kinematic viscosity. ANSYS Fluent uses the finite-volume method in order to solve conservation equations [Ansys user manual].

During the analysis, second order implicit method has been used for the transient solution. SIMPLE-type implicit algorithm is implemented for pressure-velocity coupling. The solution of the simulation is second order accurate in space and time.

The semi-circular region of the outer domain is used as the velocity inlet and the other side of the outer region has been used as the pressure outlet. External condition of the flow around all the airfoils is obtained at Re = 1000 for different angles of attack.

For the thickness distribution of NACA 4-digit airfoils, the following equation of y_t has been used [NACA Technical Memorandum 4741, 1996 & Abbott,1959],

$$y_t = \pm\frac{t/c}{0.2}\cdot\left(0.2969\cdot\sqrt{x} - 0.1260\cdot x - 0.3516\cdot x^2 + 0.2843\cdot x^3 - 0.1015\cdot x^4\right) \tag{3}$$

where xϵ [0 1] and t/c is the maximum thickness to chord ratio, which is in percentage last two digits of NACA 4-digit airfoils.

The angle of attack is defined to be positive in the clockwise direction starting from 0° to 10° with an increment of 1° per analysis. The pivot point for angles was located at the quarter chord (0.25c) from the leading edge of each airfoil.

Grid and time refinement studies

To validate the analysis, a detailed study of grid and time refinement has been carried out only on NACA 1412. These studies have been conducted for two different angles of attack, namely 5° and 10°. For grid refinement studies, three different meshes have been used as coarse, medium, and fine meshes. Node and element numbers of the domain for each mesh are enlisted in Table 1. The domain has two regions, an inner region and an outer region. The inner region is constructed with a semi-circle front end with a radius of 2.5c with a center at c/4 location of the airfoil at the upstream and a rectangular region with a width of 2.5c at the downstream. The whole inner region mesh is generated using unstructured triangular grid. The outer region is constructed with a C-type structured mesh with a radius of 25c and a rectangular design at the wake of the airfoil with a length of 30c (Figure 1). For each analysis, the airfoil is rotated in a clockwise direction for the given angles of attack to keep the wake region constant. The time increment used for grid refinement study is $\Delta t = 0.005s$. The simulations are conducted until t = 100 s and a non-dimensional time of $t^* = t \times U_\infty / c = 146$ where the free stream velocity, $U_{inf} = 0.146$ m/s and chord length, c = 0.1 m. The computational time interval is $t^* \epsilon$ [0 146] for the simulations. In this study, the main concern is to analyze the behavior of the airflow after the results reach to steady state or periodic conditions. Therefore, the initial behavior of the solution is ignored.

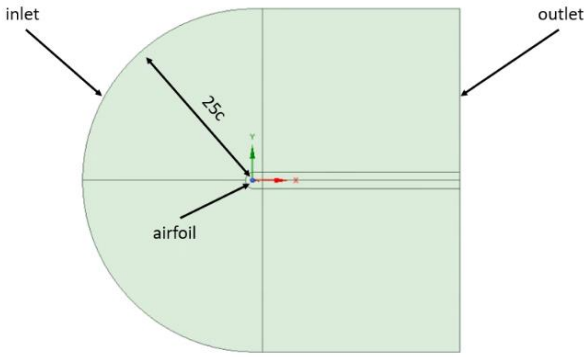

Figure 1: Computational domain

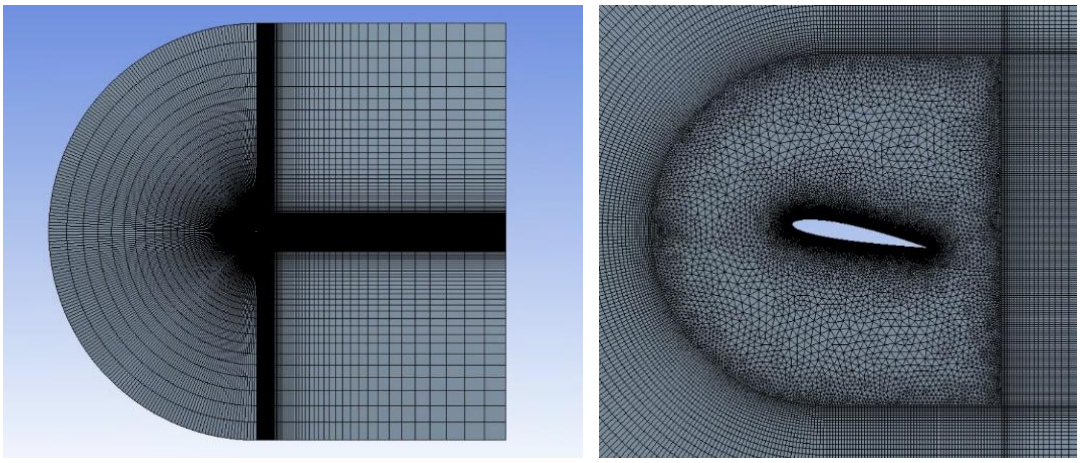

Figure 2: Meshed computational domain

Table 1: Computational mesh for NACA 1412 airfoil at α = 5° and α = 10°

Domain	Nodes around the airfoil	Total number of Elements
Coarse mesh	63923	77206
Medium mesh	93319	108638
Fine mesh	130735	146366

From the grid refinement study, it is noticed that all three meshes results in approximately same aerodynamic coefficients at the initial start region. The results reaches a quasi-steady solution at t*=19.4 stay the same throughout the whole simulation. Therefore, depending on this outcome the rest of the simulations have been conducted using medium mesh as the differences are quite negligible as shown in Figure 3.

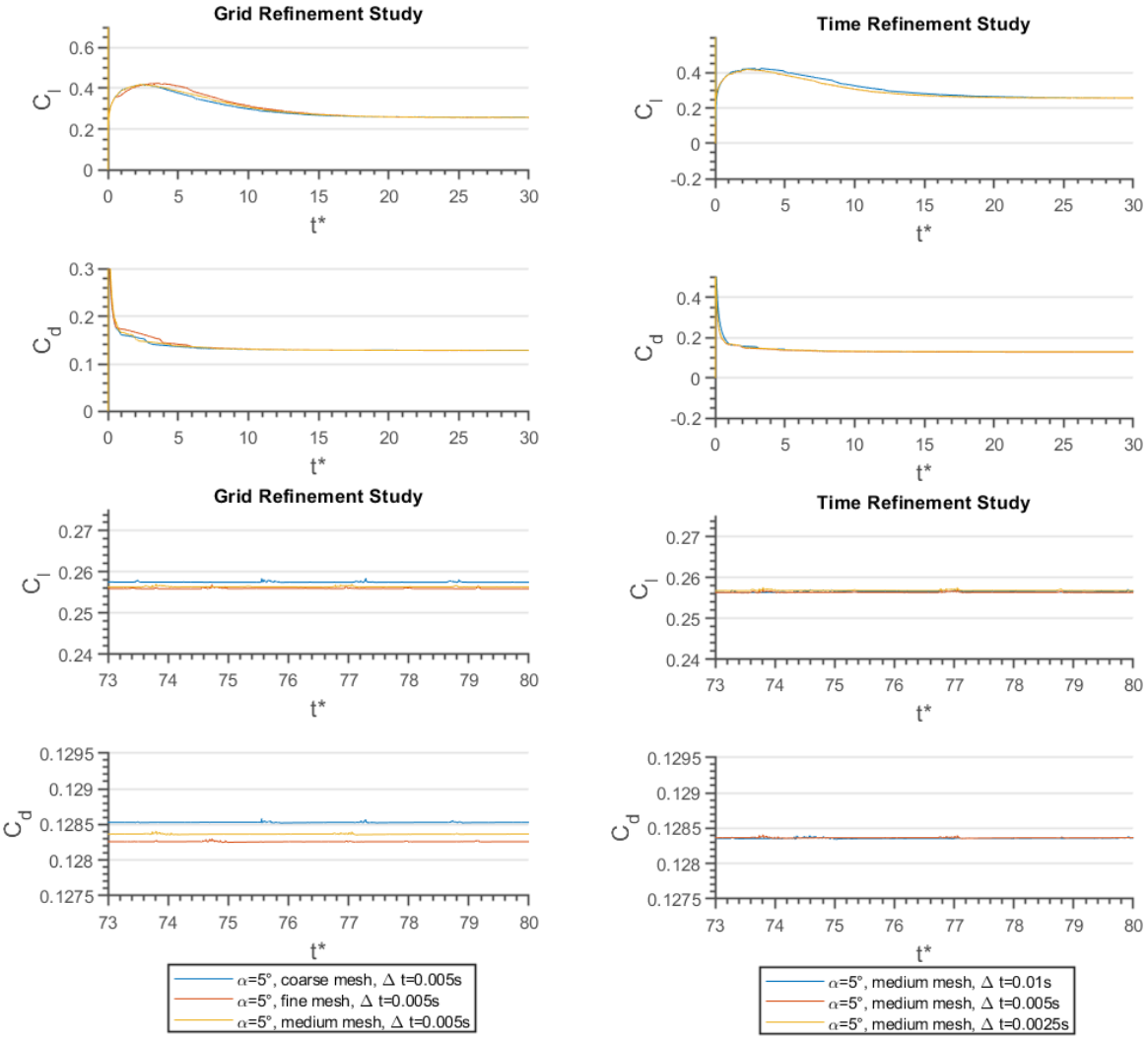

Figure 3: Instantaneous lift and drag coefficients for the grid (left column) and time (right column) refinement studies during t*ϵ [0 30] (top two rows) and during t*ϵ [73 80] (bottom two rows) for α=5°.

For α=10°, the instantaneous aerodynamic forces are also found to be very close to each other for all three meshes investigated with a phase shift due to the unsteadiness and flow separation at this angle of attack. However the period of the oscillation and amplitude of the oscillation are very close to each other for all three mesh configurations investigated

Similarly, a time refinement study has also been conducted with the medium mesh for time increments (Δt) of 0.01s, 0.005s, and 0.0025s.

At α=10°, the results for time step 0.01s phases out at t*=16.1 and follow a cyclic pattern throughout the simulation. Phase shifts are visible between the three time increments but the frequency and the amplitude of the oscillations are close to each other.

All the results for grid and time refinement studies at α=5° and α=10° for time intervals of t*ϵ [0 30] and t*ϵ [73 80] are represented in Figure 3 and Figure 4, respectively.

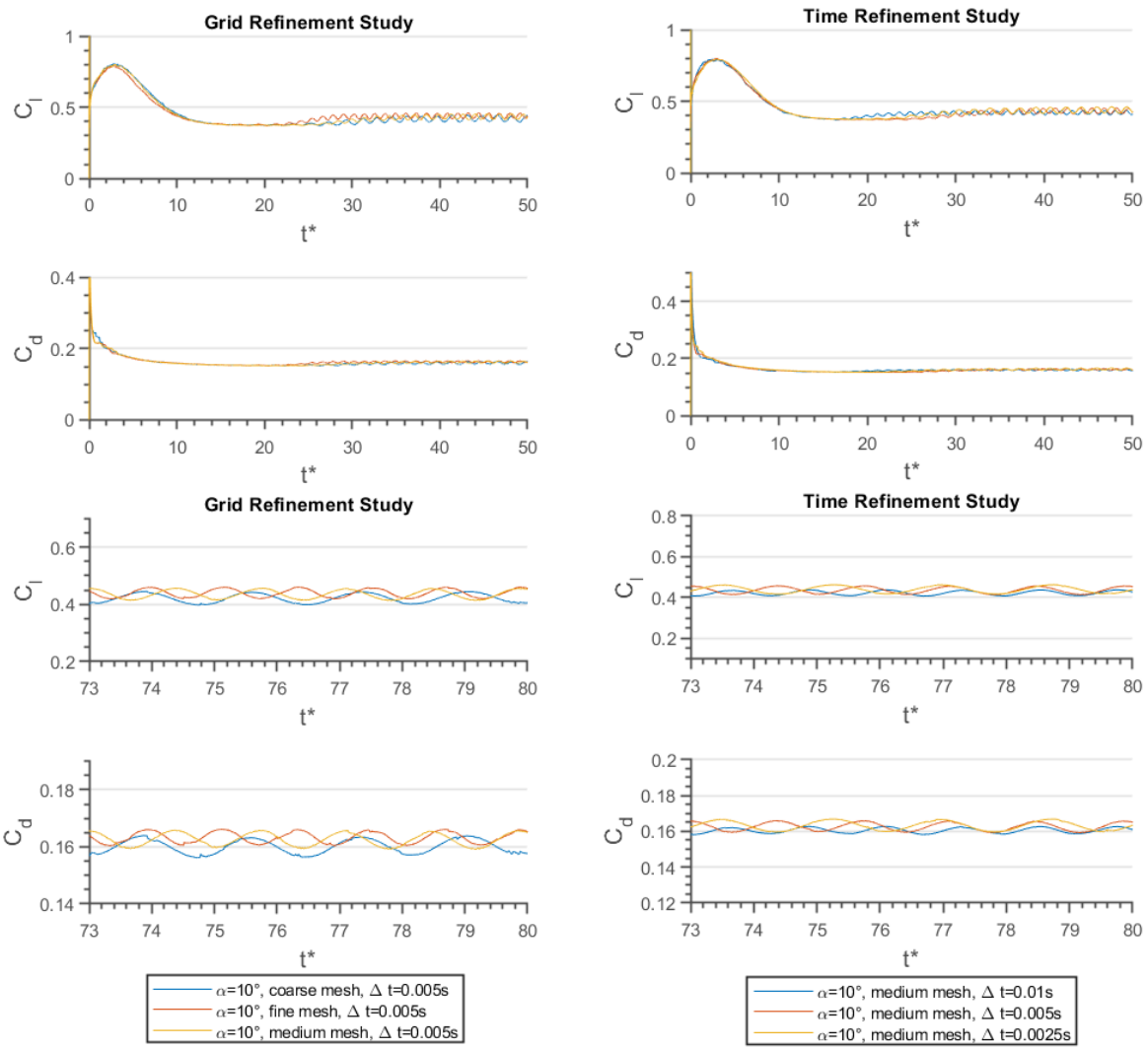

Figure 4: Instantaneous lift and drag coefficients for the grid (left column) and time (right column) refinement studies during t*ϵ [0 30] (top two rows) and during t*ϵ [73 80] (bottom two rows) for α=10°.

Validation study

The results of the current study are also compared with the UNS2d simulations conducted by Kunz et al 2003 for NACA 4402 airfoils at Re=1000 for angles of attack ranging from 0° to 10° for fully laminar flow (Figure 5).

In Figure 5, similar lift curve pattern is observed and both analyses indicate similar reduction in the lift curve slope as well for the mean lift coefficient. In general, the comparison between these two analyses provides a validation for the current study for low angles of attack. As the unsteadiness in the flow increases, the aerodynamic force coefficients are found to differ at higher angles of attack of 9° and 10°. This part will further be studied.

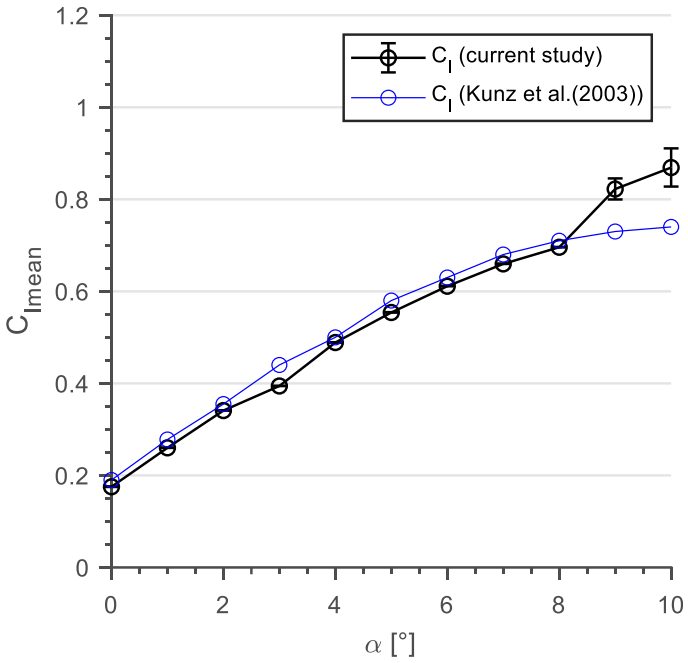

Figure 5: Mean lift coefficient and comparison with literature data at Re=1000.

RESULTS AND DISCUSSION

All the solutions are obtained using different angles of attack ranging from 0° to 10° with an increment of 1°. The main objective of the study is to observe the effect of the camber on the instantaneous aerodynamic performance of the airfoils at a very low Reynolds number.

Mean aerodynamic coefficients

Figure 6 shows the instantaneous aerodynamic coefficients of NACA 1412 for angles of attack 0° to 10° with an increment of 1°. Figure (a) contains the instantaneous lift coefficients against non-dimensional time step t*. At the starting point (t*=0 to 15), a spike is observed which was expected as the simulation starts with an initial assumption that is far from the stable value. Then all the solutions start to converge at t*= 32 and gradually converge afterwards. An oscillatory behavior is observed for instantaneous C_l values for angle of attack of 9° and 10°. This results a vortex mode shape change from continuous vortex shedding to an alternating vortex shedding configuration (Kurtulus, 2015, 2016).

Similarly, Figure 6b shows the instantaneous C_d value for different angles of attack ranging from 0° to 10°. The values start to converge at t*=32 and only oscillations are observed for angles of attack 9° and 10°.

The mean lift coefficient ($\overline{C_l}$) and mean drag coefficient ($\overline{C_d}$) for different angles of attack for 0° to 10° at Re=1000 for NACA 1412 is presented in Figure 7 with error bars denoting the minimum and maximum oscillations of the unsteady amplitudes in the interval where the mean values (presented as black circles) are considered. A gradual increase in lift curve is noticed as the angle of attack increase from 0° to 10° which is different that the high Reynolds number lift coefficient curves having a linear trend until the stall angle.

Figure 8 to Figure 11 show the results obtained for NACA 2412 and NACA 3412 including both instantaneous and mean lift coefficient and drag coefficient for different angle of attack ranging from 0° to 10° for Re=1000.

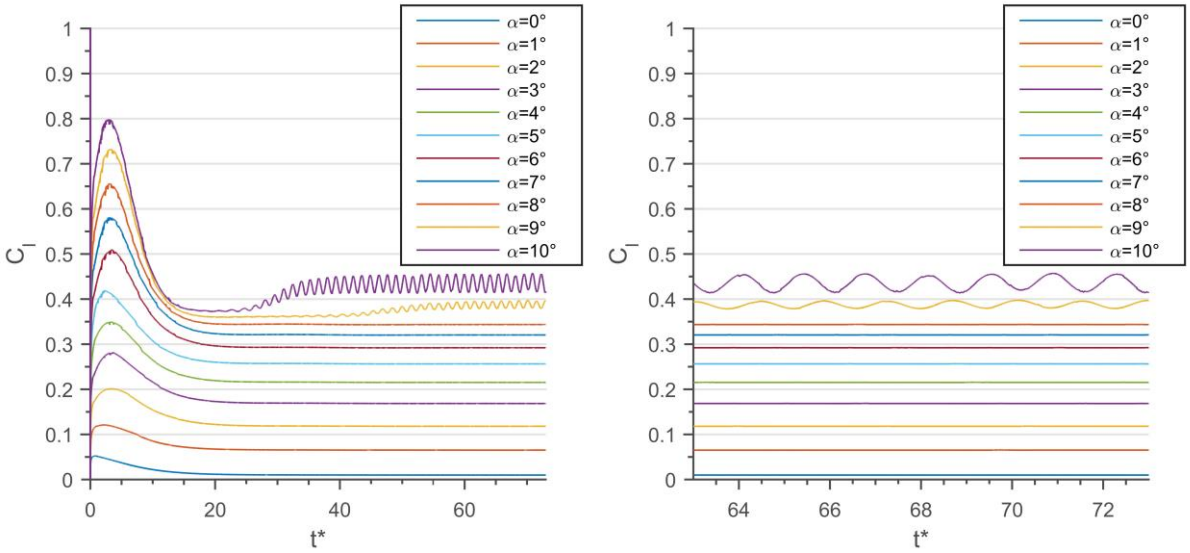

a) Instantaneous lift coefficient

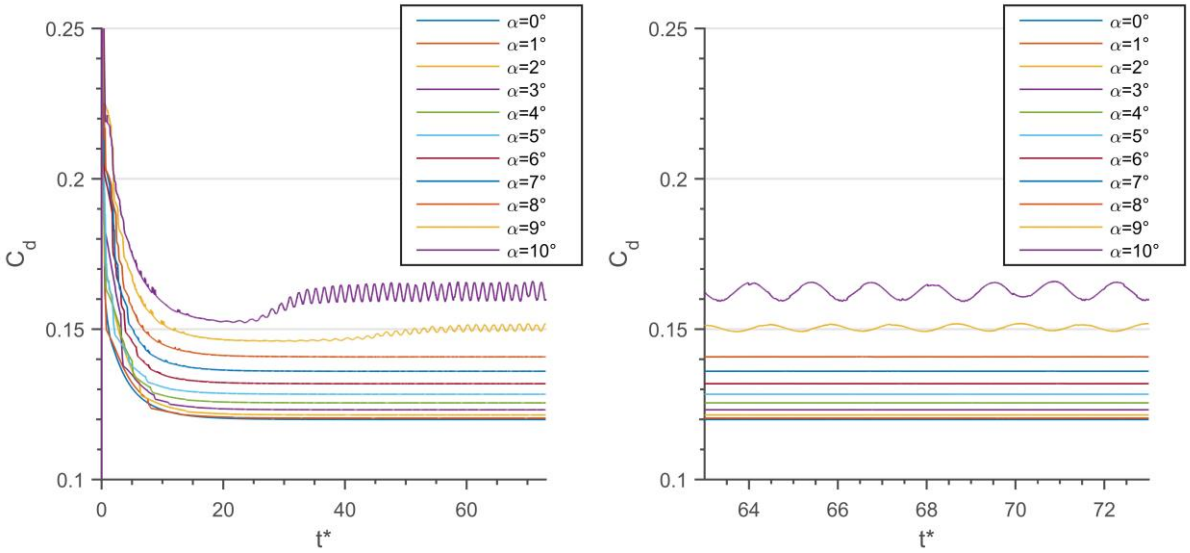

b) Instantaneous drag coefficient

Figure 6: Instantaneous aerodynamic coefficients of NACA 1412 at different angles of attack at Re=1000.

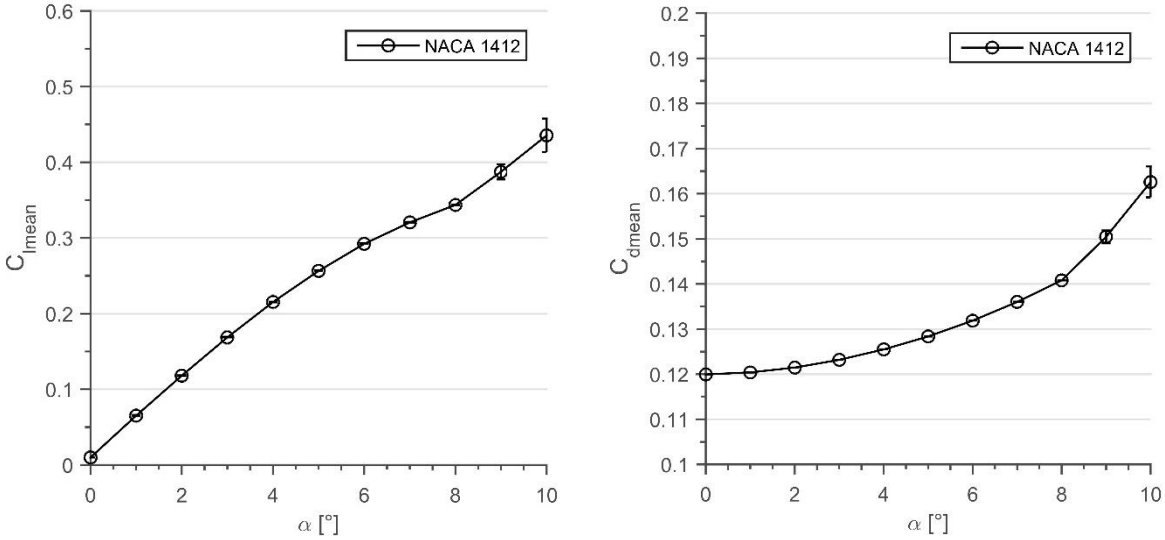

Figure 7: Mean aerodynamic force coefficients of NACA 1412 at different angles of attack.

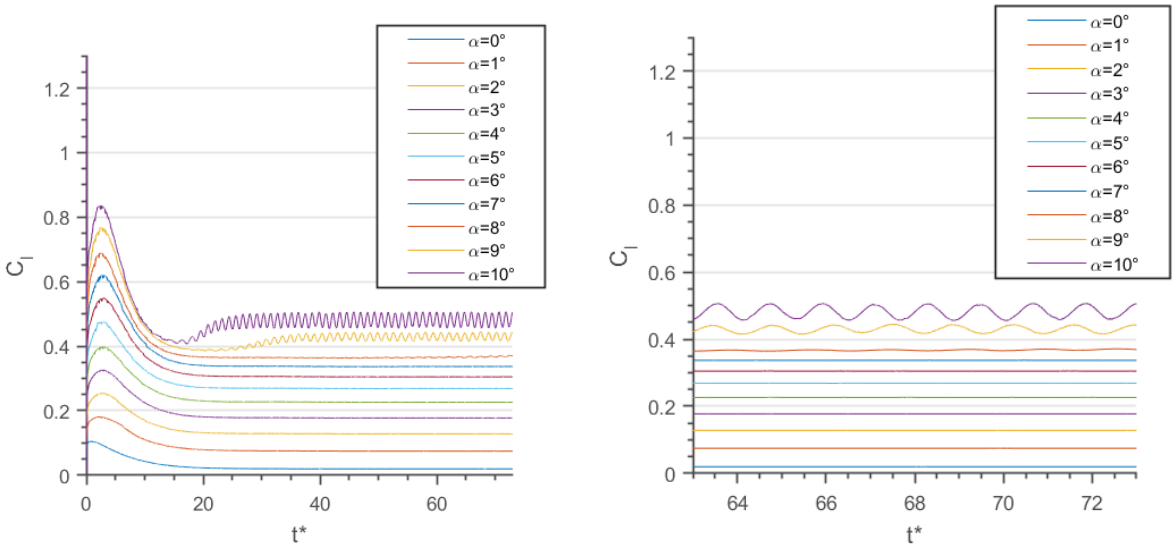

a) Instantaneous lift coefficient

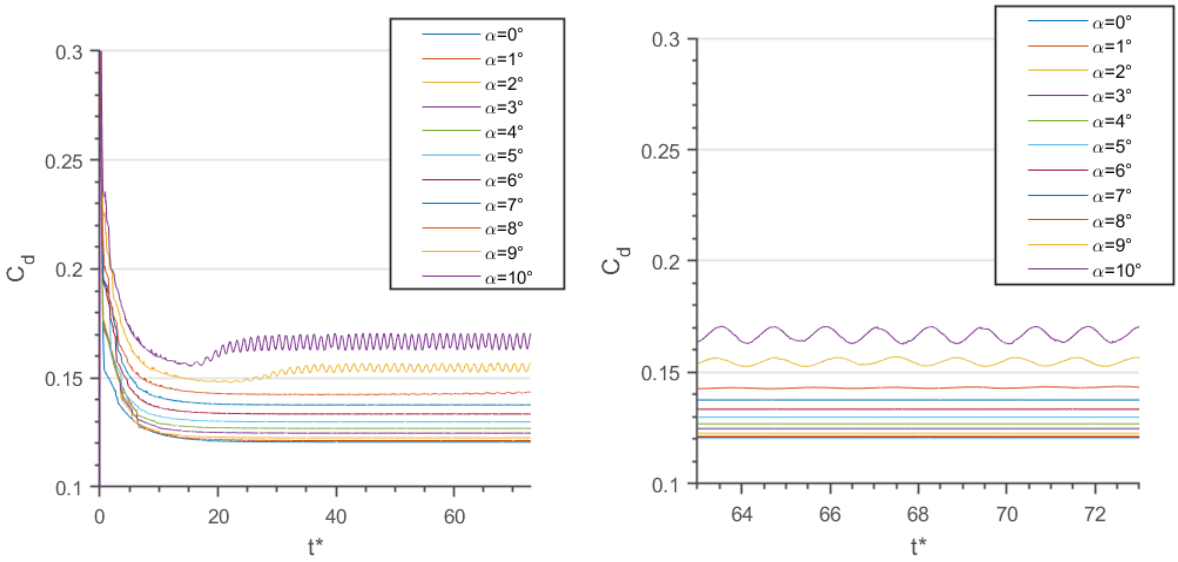

b) Instantaneous drag coefficient

Figure 8: Instantaneous aerodynamic coefficients of NACA 2412 at different angles of attack at Re=1000

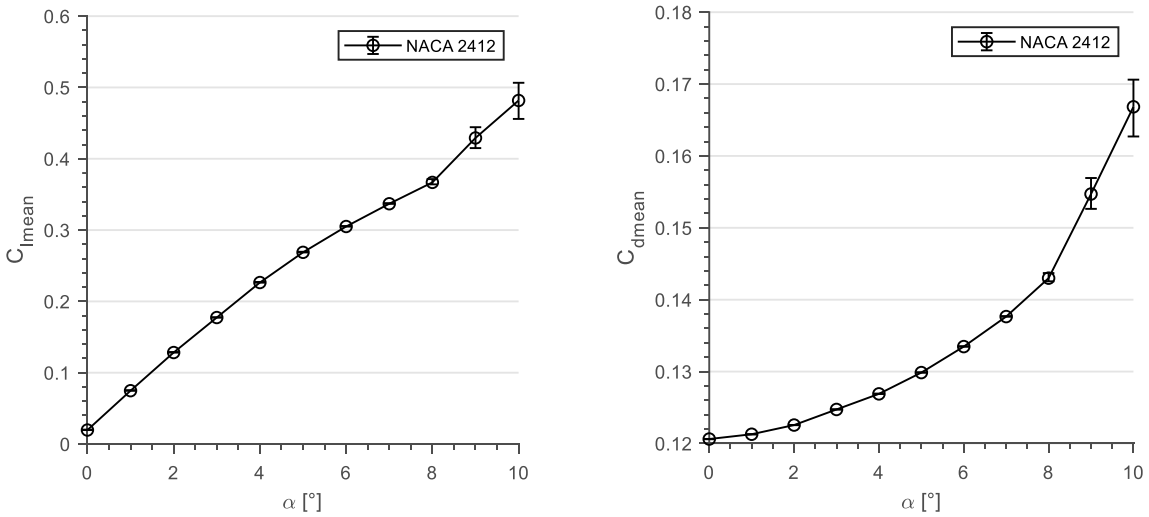

Figure 9: Mean aerodynamic force coefficients of NACA 2412 at different angles of attack.

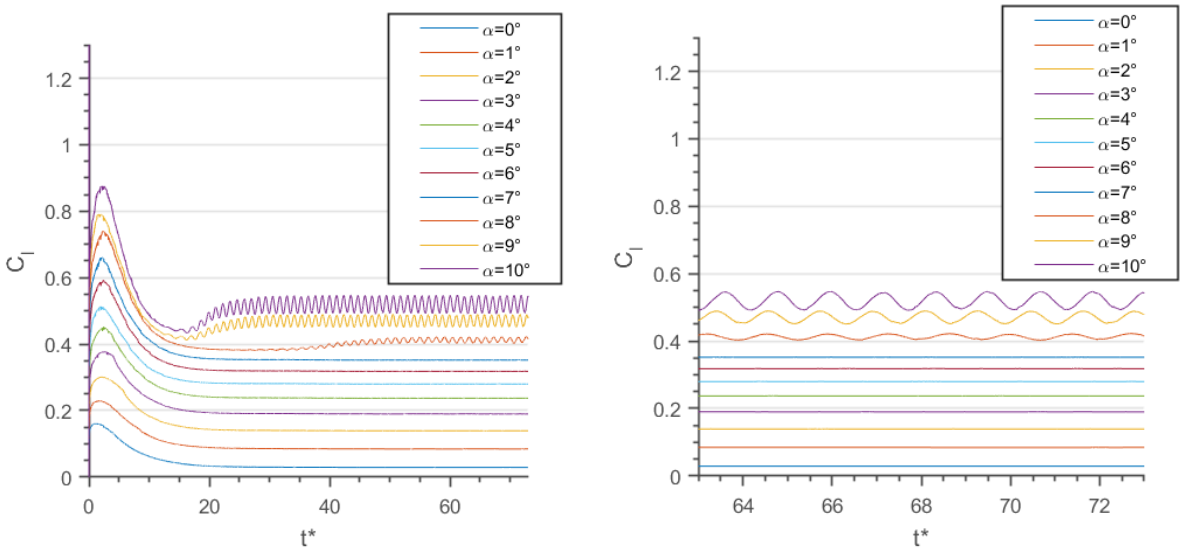

a) Instantaneous lift coefficient

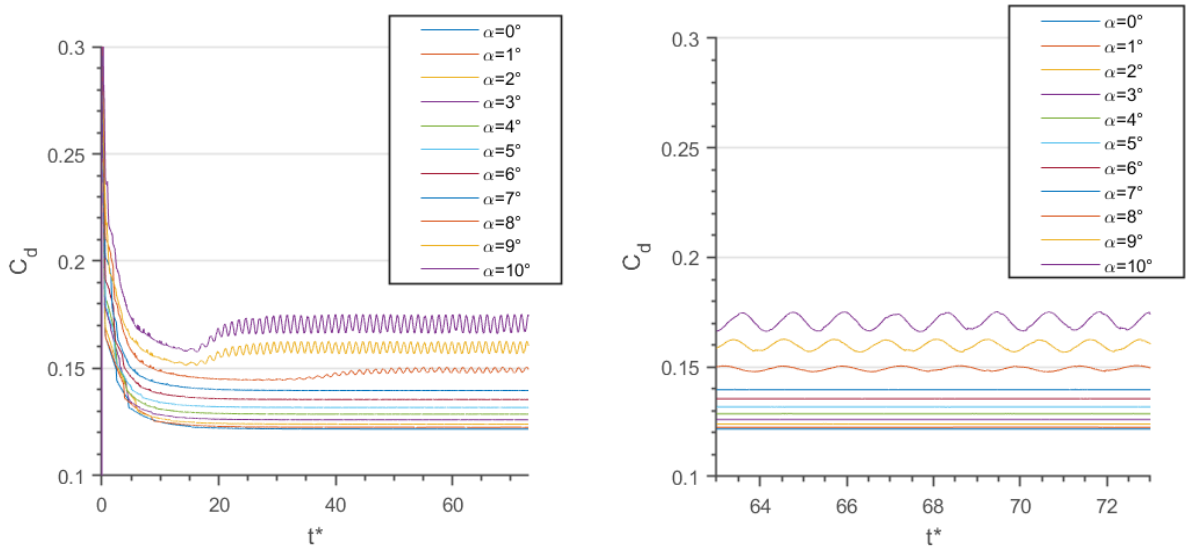

b) Instantaneous drag coefficient

Figure 10: Instantaneous aerodynamic coefficients of NACA 3412 at different angles of attack at Re=1000.

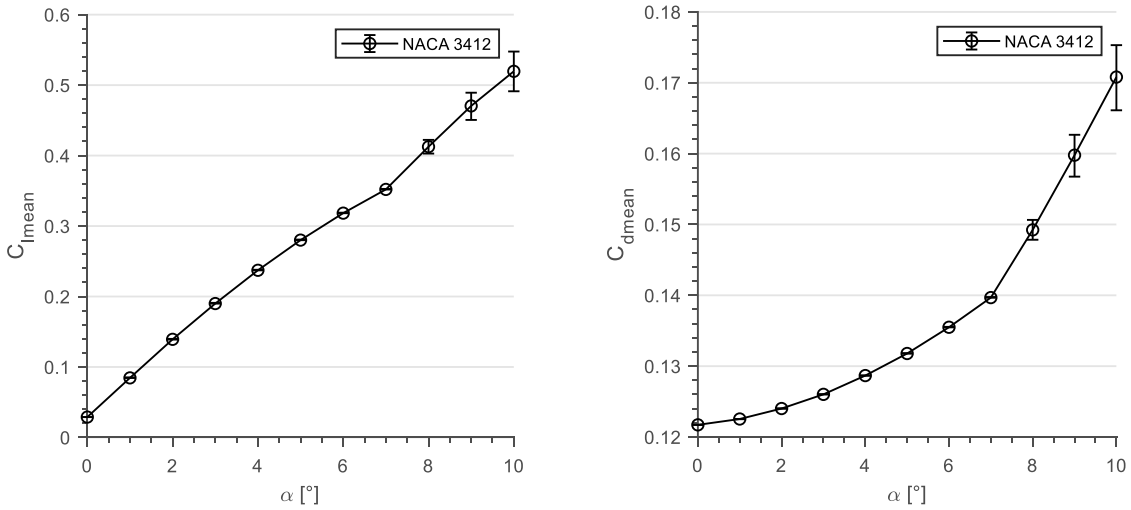

Figure 11: Mean aerodynamic force coefficients of NACA 3412 at different angles of attack.

Figure 12 shows a comparison of aerodynamic coefficients between the three NACA airfoil profile NACA 1412, NACA 2412, and NACA 3412 at Re=1000 for different angles of attack. It can be noticed that as the maximum camber of the airfoils increases, the mean lift coefficient increases but so as the drag coefficients. As the angle of attack increases, the discrepancy between the mean aerodynamic force coefficients increases. At angle of attack of 10°, each 2% increase leads to around 7 to 9% increase in mean lift coefficient and around 2.5% in mean drag coefficient. It's a considerable trade off in terms of MAVs wing design.

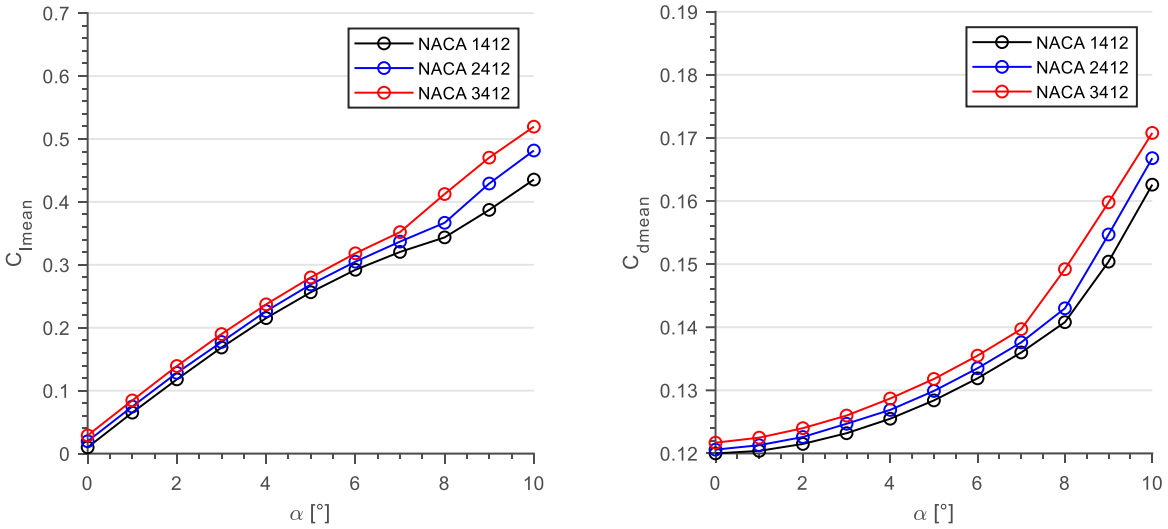

Figure 12: Comparison of mean aerodynamic coefficients for different airfoils.

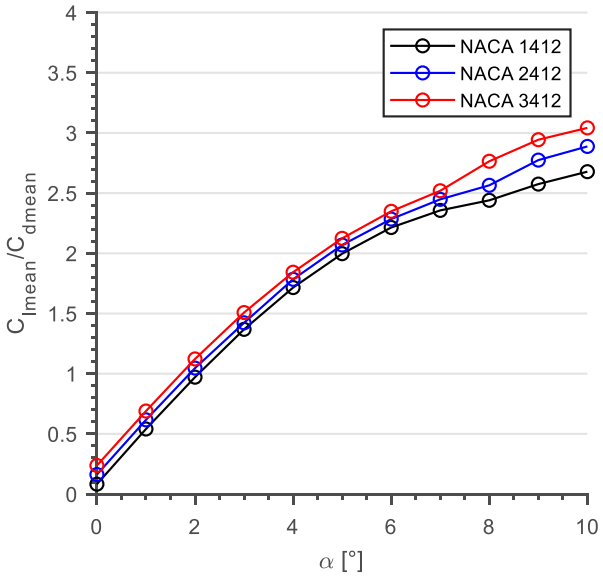

Figure 13: Comparison of mean C_l/C_d value for different airfoils.

A clear view of how $\overline{C_l}/\overline{C_d}$ value changes with respect to angle of attack is presented in Figure 13. It can be observed that as the camber increases, mean C_l/C_d also increases. At α=10°, NACA1412, NACA2412, and NACA3412 have mean C_l/C_d values of 2.6784, 2.8879, and 3.0422, respectively showing an around 5-7% of change per 1% maximum camber increase.

Instantaneous Pressure Distributions

A relative comparison of instantaneous pressure distributions around the airfoils are presented in Figure 14 and 15 for α=9° and 10° as these two angles of attack show unsteady behavior. It can be observed from the figures that as the angle of attack is increasing, the negative pressure at the leading edge is increasing as well As the camber increases, the leading-edge pressure suction value is also observed to decrease.
The instantaneous streamlines are also presented for the cases investigated on Figure 14 and Figure 15 for α=9° and 10°, respectively.

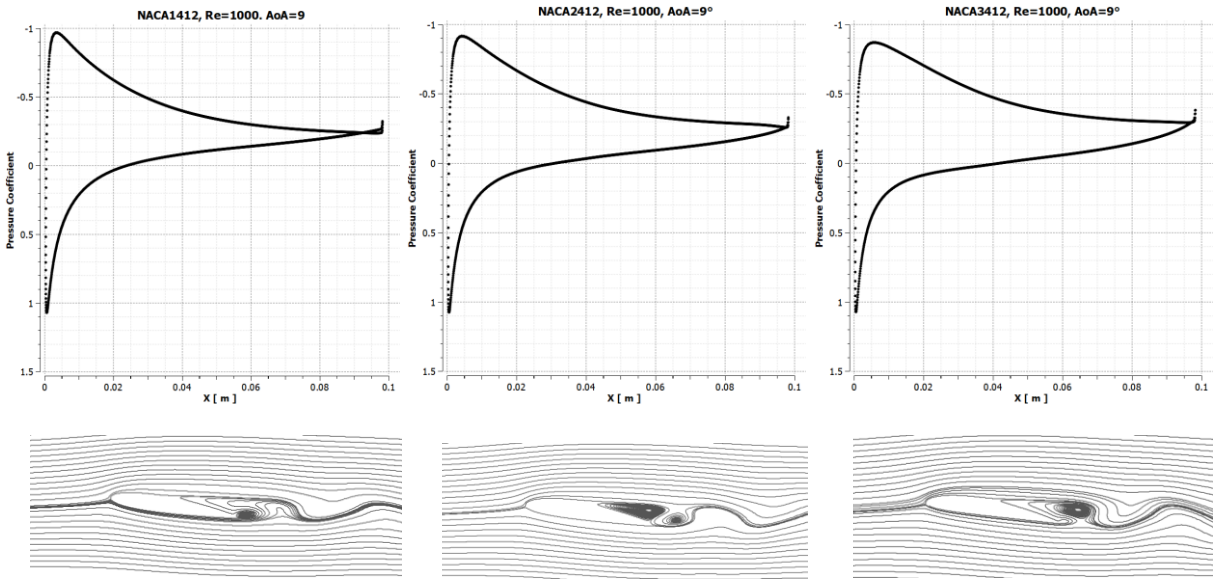

Figure 14: Instantaneous pressure distributions and streamlines around NACA1412, NACA2412, and NACA3412 at α = 9° at t*=73.

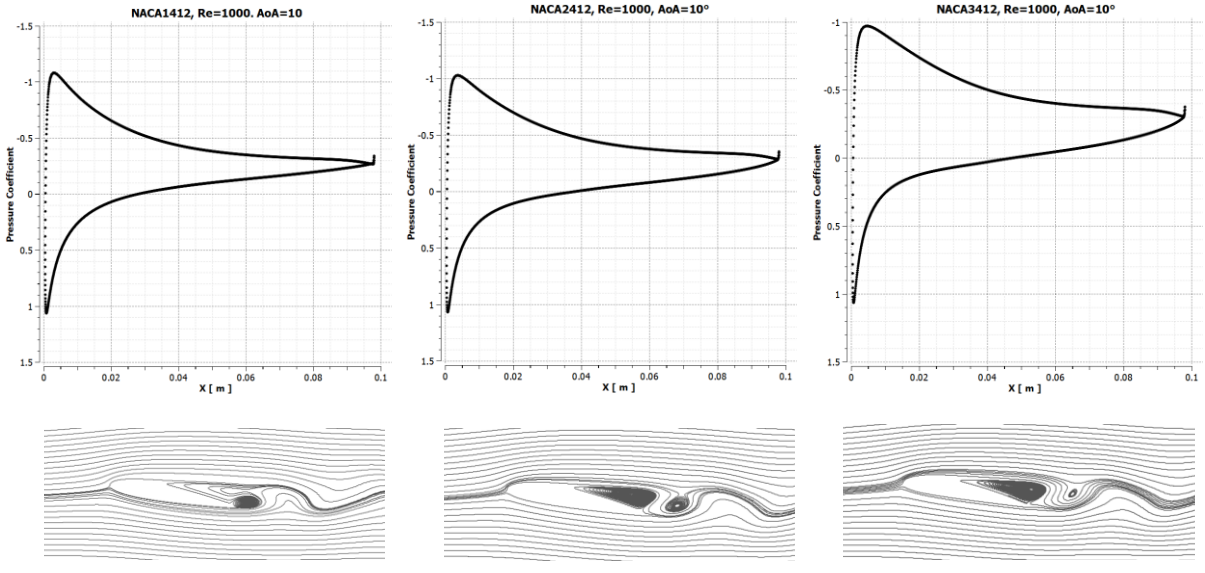

Figure 15: Instantaneous pressure distributions and streamlines around NACA1412, NACA2412, and NACA3412 at α = 10° at t*=73.

Vortex patterns are highly dependent on angle of attack and also moderately to the camber distribution. In order to understand the patterns, instantaneous streamlines are compared for each airfoil at α=1°, 5°, and 7° for Re=1000 in Figure 16. The trailing edge vortex is found to grow quickly at higher cambered airfoils. The trailing edge vortex is highly visible for NACA 3412 at α=1°compared to NACA 1412 and NACA 2412 airfoils as shown in Figure 16a.

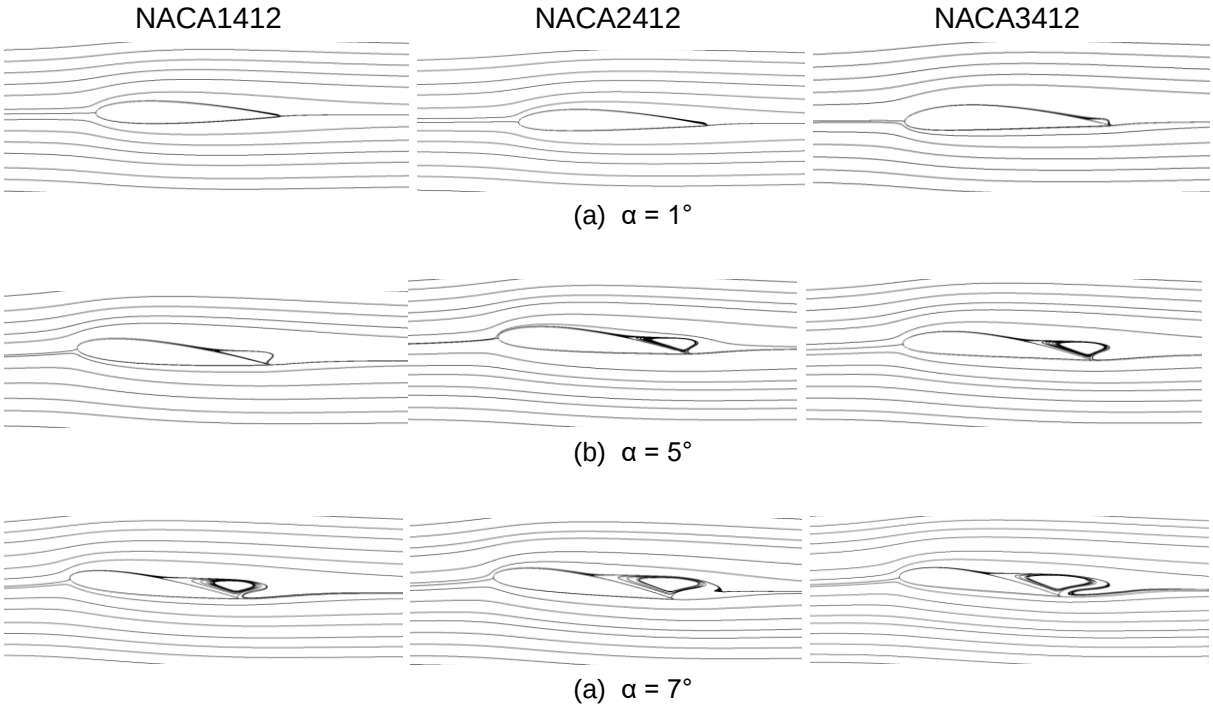

Figure 16: Streamlines of mean velocity field for angels of attack 1°, 5° and 7° for NACA1412, NACA2412, and NACA3412 for Re=1000.

Skin Friction Coefficient

At very low Reynolds numbers, due to viscous effects in the flow, the boundary layer becomes very thick on the airfoil and flow separation may occur even at smaller angles of attack. Therefore, the study of flow separation is very important in this kind of analysis where Reynolds number is very low.

Flow separation positions can be determined by observing the skin friction coefficient values. In the position of flow separation skin friction coefficient will be zero as there will be no attachment to the flow with the airfoil surface.

Flow separation positions may vary due to maximum camber, angle of attack or Reynolds number. A brief comparison between different airfoils with different maximum camber distributions at angle of attack of 9° and 10° are represented in Figures 17 and 18. The separation points are marked with red dots on airfoil profiles where skin friction coefficient is equal to zero. It can be noticed that as the maximum camber increases, the initial flow separation point shifts towards rear side.

The angle of attack plays the main role in the flow separation positions. As the angle of attack increases the flow separation point shifts towards the leading edge.

Therefore, increasing maximum camber can be a way of delaying flow separation position towards the trailing edge when designing MAV wings.

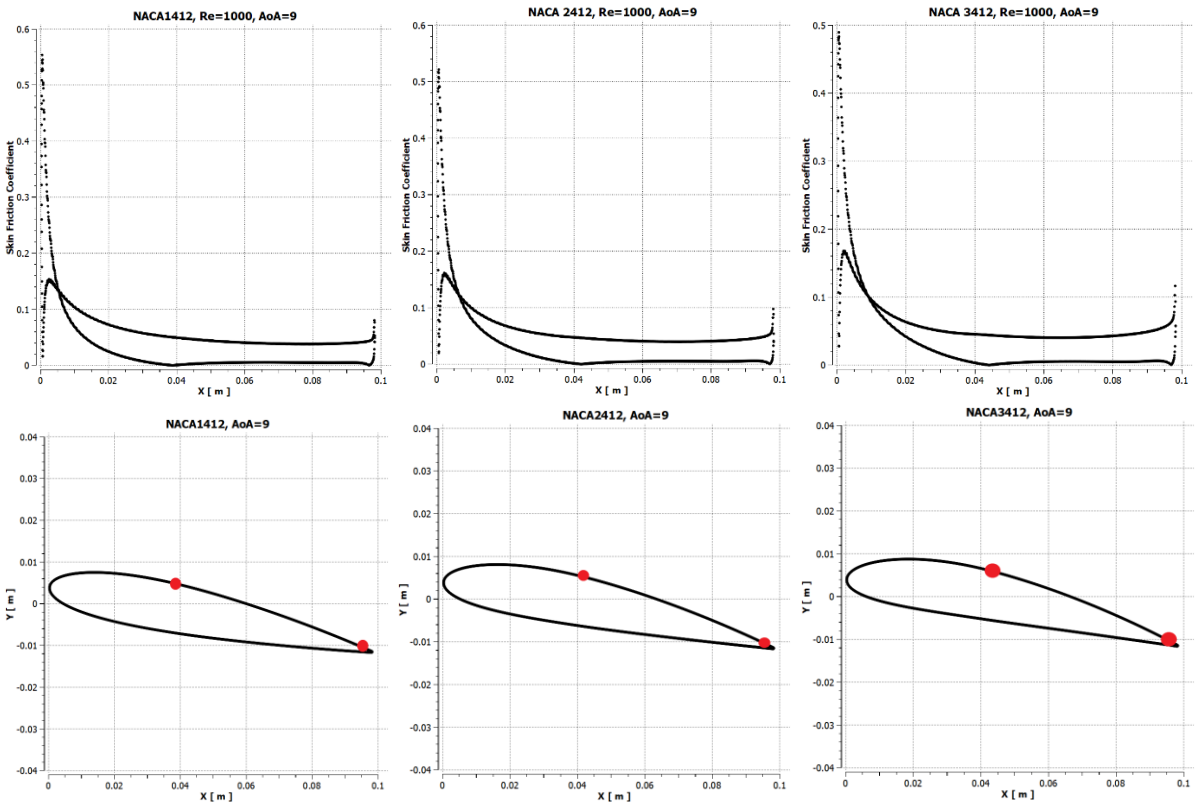

Figure 17: Skin friction coefficient and separation point on NACA1412, NACA2412, and NACA3412 at α = 9°.

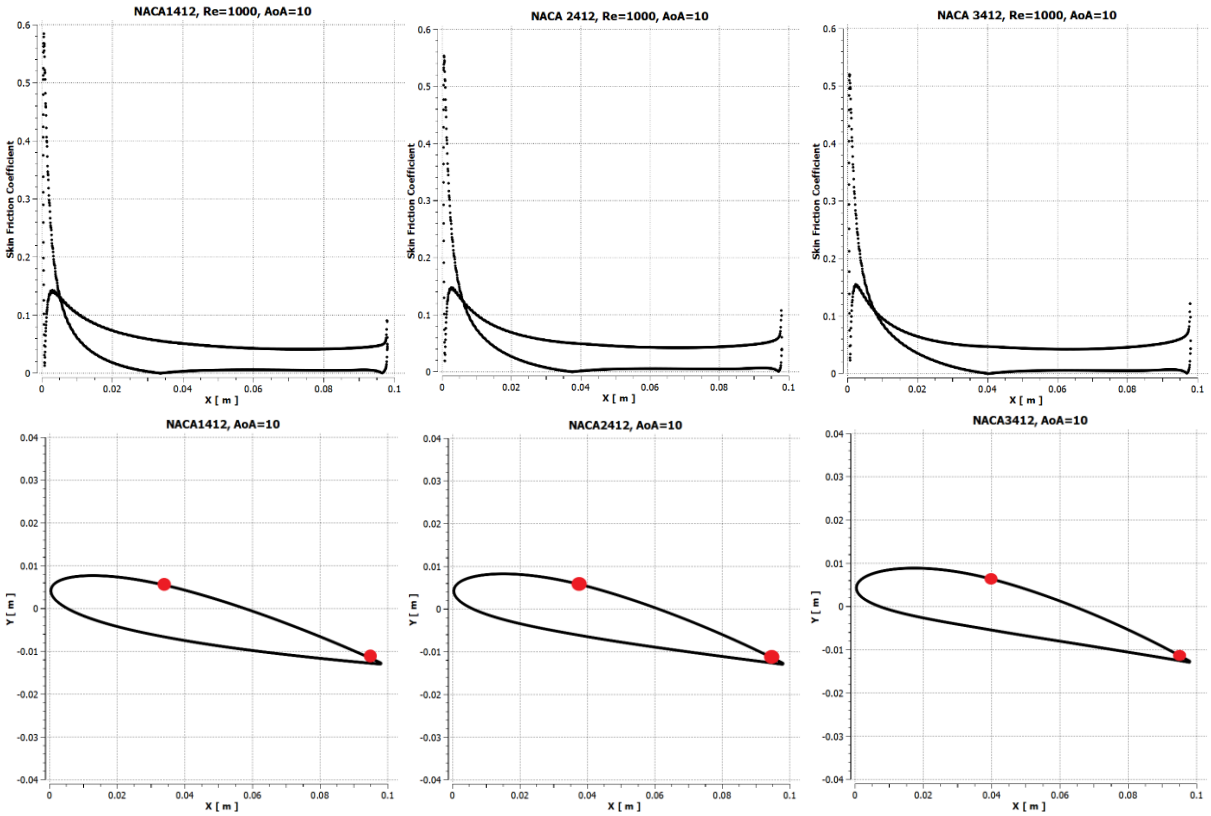

Figure 18: Skin friction coefficient and separation point on NACA1412, NACA2412, and NACA3412 at α = 10°.

Vortex shedding patterns of the Airfoils

Vortex shedding patterns need to be observed in order to distinguish also the unsteady flow behavior. At angle of attack less than 8° the vortices are continuous and there is no any alternating vortex shedding pattern at the wake of the airfoil. Figure 19 shows the instantaneous vorticity contours at α=7° which is same as the mean vorticity contours during a period without any alternating vortices. But at angles larger than 8° alternating vortex shedding are visualized at the trailing edge of the airfoils (Figure 20 and Figure 21). Two counter rotating vortices are produced where upper vortices rotate in the clockwise direction and lower vortices rotate in the counterclockwise direction.

α = 7°

NACA 1412

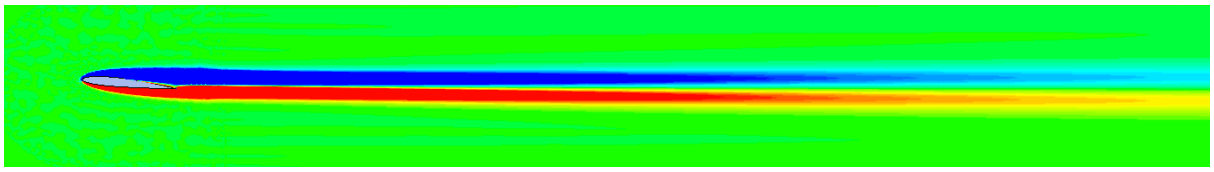

NACA 2412

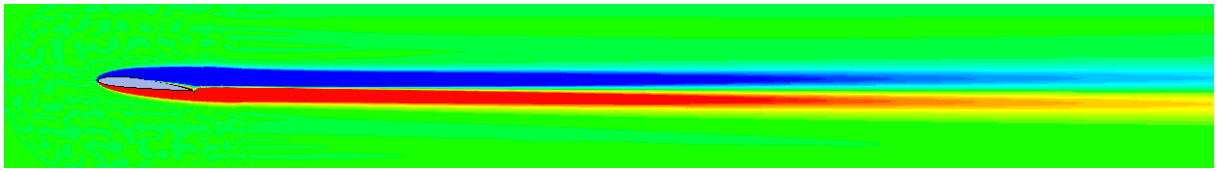

NACA 3412

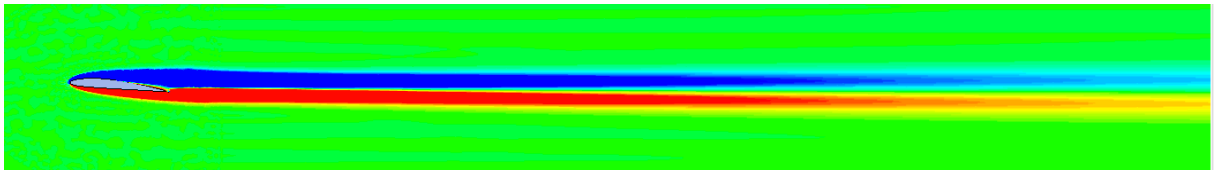

Figure 19: Instantaneous vorticity patterns for NACA1412, NACA2412, and NACA3412 at α = 7° at t*=73.

α = 9°

NACA 1412

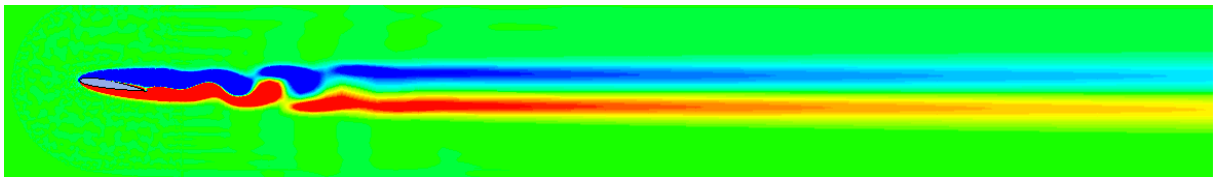

NACA 2412

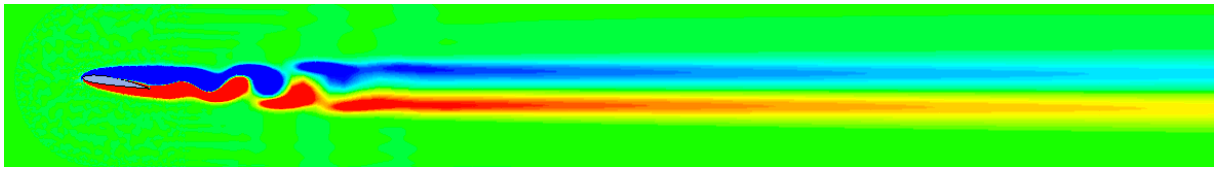

NACA 3412

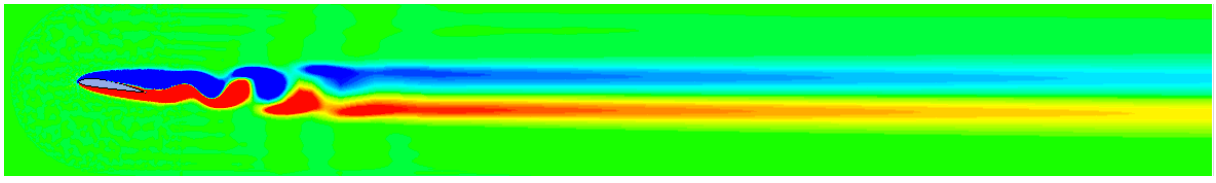

Figure 20: Instantaneous vorticity patterns for NACA1412, NACA2412, and NACA3412 at α = 9° at t*=73.

α = 10°

NACA 1412

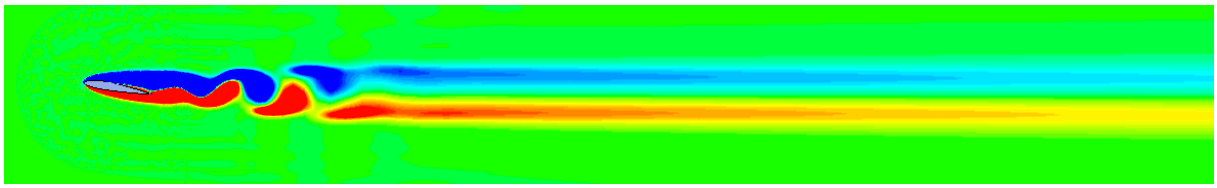

NACA 2412

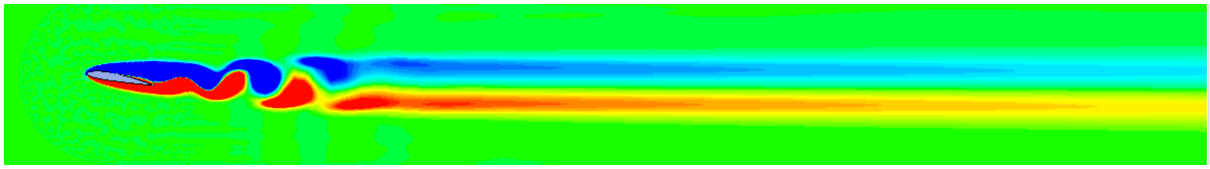

NACA 3412

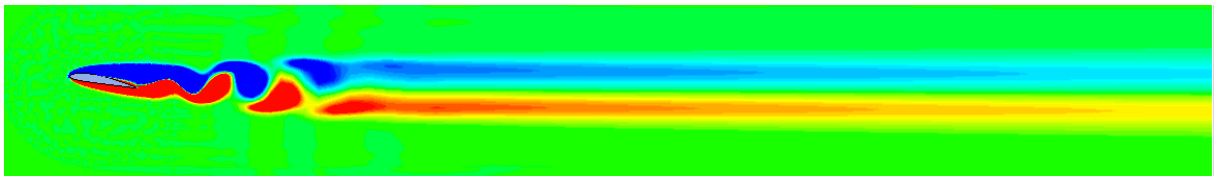

Figure 21: Instantaneous vorticity patterns for NACA1412, NACA2412, and NACA3412 at α = 10° at t*=73.

CONCLUSION

This article represents the aerodynamic behavior of the flow around cambered airfoils at a very low Reynolds number (Re=1000) as angle of attack increases from 0° to 10° with an increment of 1° for each simulation which are of interest for Micro Air Vehicles (MAVs). The influence of the angle of attack to instantaneous and mean aerodynamic coefficients, pressure distributions and streamlines are discussed.

A comparison in terms of aerodynamic coefficients between three different cambered airfoils, namely NACA 1412, NACA2412, and NACA 3412 is presented to understand the effect of cambered airfoil at very low Reynolds number. From the analyses, it can be noticed that as the camber increases, the mean lift coefficient increases by around 7-9% and mean drag coefficient increases by around 2.5% at angle of attack of 10°.

Furthermore, instantaneous pressure distribution and streamline flow over different cambered airfoils are discussed. As the maximum camber increases, the suction pressure at the leading edge is found to decrease. The instantaneous streamlines for different angles of attack have been demonstrated in order to understand the vortex structure for different cambered airfoils. Alternating vortex shedding is found to occur at angles bigger than equal to 9° for the airfoils investigated at Re=1000. The vorticity flow field is found to be continuous for angles of attack smaller than equal to 8°.

The skin friction coefficients have been analyzed to understand the effect of cambered airfoils on flow separation position. Flow separation points are found to shift towards the trailing edge as maximum camber of the airfoil increases. However, as the angle of attack increases, the flow separation points shift towards the leading edge.

References

Abbott, I. H., and von Doenhoff, A. E. (1959) Theory of Wing Sections, Dover, New York, ISBN 0-486-60586-8.

ANSYS Fluent User guide, ANSYS Inc.

Gopinath A. K. and Jameson, A. (2006) Application of the Time Spectral Method to Periodic Unsteady Vortex Shedding, AIAA Paper, 0449.

Kang, C. K. and Shyy, W. (2013) Scaling law and enhancement of lift generation of an insect-size hovering flexible wing, J R Soc Interface, 10: 20130361.

Kunz, P. and Kroo, I. (2000) Analysis and Design of Airfoils for Use at Ultra-Low Reynolds Numbers,Proc. AIAA Fixed, flapping and rotating wing aerodynamics at very low Reynolds numbers conference, edited by T. J. Mueller, Notre Dame, June 5-7, pp. 35-60.

Kunz, P. J., (2003) Aerodynamics and Design for Ultra-Low Reynolds Number Flight.

Kurtulus, D. F., Farcy, A. and Alemdaroglu, N. (2005) Unsteady Aerodynamics of Flapping Airfoil in Hovering Flight at Low Reynolds Numbers, AIAA Paper,1356.

Kurtulus, D.F., David, L., Farcy, A. and Alemdaroglu, N. (2008) Aerodynamic Characteristics of Flapping Motion in Hover. Experiments in Fluids, 44, 23–36.

Kurtulus D.F. (2015) On the unsteady behavior of the flow around NACA 0012 airfoil with steady external conditions at Re=1000, International Journal of Micro Air Vehicles, Vol 7, No 3, pp 301-326.

Kurtulus D.F. (2016) On the wake pattern of symmetric airfoils for different incidence angles at Re=1000, International Journal of Micro Air Vehicles, Vol 8, No:2, pp. 109-139.

NACA Technical Memorandum 4741 (1996) Computer Program To Obtain Ordinates for NACA Airfoils.

Ohmi K., Coutanceau, M., Loc T. P. and Dulieu A. (1990) Vortex formation around an oscillating and translating airfoil at large incidences, J. Fluid Mech, 211, 37-60.

Ohmi K., Coutanceau, M., Daube, O. and Loc, T. P. (1991) Further experiments on vortex formation around an oscillating and translating airfoil at large incidences, J. Fluid Mech, 225, 607-630.

Ol, M.V., Eldredge J. D., Wang C. (2009) High-Amplitude Pitch of a Flat Plate: An Abstraction of Perching and Flapping, International Journal of Micro Air Vehicles, 1(3), 203-216.

Platzer, M. F., Jones, K. D., Young, J. and Lai, J. C. S. (2008) Flapping-Wing Aerodynamics: Progress and Challenges, AIAA Journal, 46 (9), 2136–2149.

Shyy, W., Lian, Y., Tang, J., Viieru, D., and Liu, H., (2008) Aerodynamics of Low Reynolds Number Flyers, New York: Cambridge Univ. Press, 2008.